

Modular Continuum Robotic Endoscope Design and Path Planning

Yi Chen, Jiahui Liang and Ian W. Hunter

Abstract—Robotic endoscopes have the potential to help endoscopists position tools during procedures, to propel the endoscope to the desired position, to automate functions and to prevent perforations during procedures. This paper outlines the modular architecture for a continuum robotic endoscope with multiple bending segments along the length of the endoscope. Each of the segments is modular, containing a set of actuation motors that drive short cables in the continuum segments. Each modular segment of the robot is 15 mm in diameter, can turn 180 degrees and has a turning speed ranging from 35 to 250 degrees per second. The robot is composed of seven of these modular segments, has 14 degrees of freedom, is 0.91 m long and has a mass of 157 grams. The implementation for the mechanical, electrical, and software design is described and the robotic endoscope bending motions are sensed, simulated and controlled using kinematic models. Lastly, path planning trajectories of the endoscope segments are designed and coordinated to help propel the robot forward in an uncoiling motion and in a follow-the-leader fashion along a path that emulates simplified turns in a colon. We show that the robotic endoscope is able to exert less force on the walls of the colon emulation path, enable automated insertion into the patient, and execute colon wall avoidance and linear scanning motions not available in conventional endoscopes.

I. INTRODUCTION

FLEXIBLE endoscopy procedures such as colonoscopies are important for diagnostic and therapeutic treatment of colon cancer. Robotic endoscope designs can potentially improve the ability of endoscopists to position the endoscope, decrease the chance of perforation of the colon, and automate functions so that procedures are easier to complete with a single person. Most commercial endoscopes have a simple bending tip that is driven with Bowden cables down the endoscope body. Automating these systems can be difficult due to the reaction forces and frictional forces generated by tension on the Bowden cables. For these reasons, developing positioning or force output controllers for long cable drive systems and tendon drives are still an ongoing field of research [1]. Several techniques for robotically actuating the bending tip of an endoscope to avoid the use of long control cables have also been developed including using electric motors [2], [3], [4], shape memory alloys, pneumatics, and other combined techniques [5].

When a colonoscopy is conducted, it is sometimes difficult to maneuver the endoscope to the end of the colon at the cecum due to the shape of the colon, resulting in incomplete colonoscopies. Some methods that could help improve this

process is the use of a crawling system [6], [7], [8], [9], [10], or double-balloon actuation system [11] to move the endoscope down the colon [12]. These strategies require actively grabbing the walls of the colon and could potentially cause abrasion. Snake-like robot designs [13], [14], [15], [16] have also been considered for this application. While snake-like robotic endoscopes use rigid motorized joints, continuum bending robots have the advantage that they can complete relatively large 180° radius bends with a single actuator without producing many discrete corners. For the same number of actuators, a continuum design can also be longer allowing the whole length of the endoscope to be populated with bending segments and not just the tip.

Some continuum endoscope designs, including Neoguide [17], [18], have multiple bending points [19] along the length which are driven by several sets of cables with actuators located at the end. Because of the large number of cables in multi-bend designs, the endoscope becomes thicker the further away from the tip. Follow-the-leader designs [20], [21] use a single set of cables to create several bends along the length as the endoscope is advanced. These designs can be used to avoid colon walls thereby minimizing abrasion. However, these multi-bend and follow-the-leader designs cannot readily increase the number of bending segments and require complex drive systems at the proximal end.

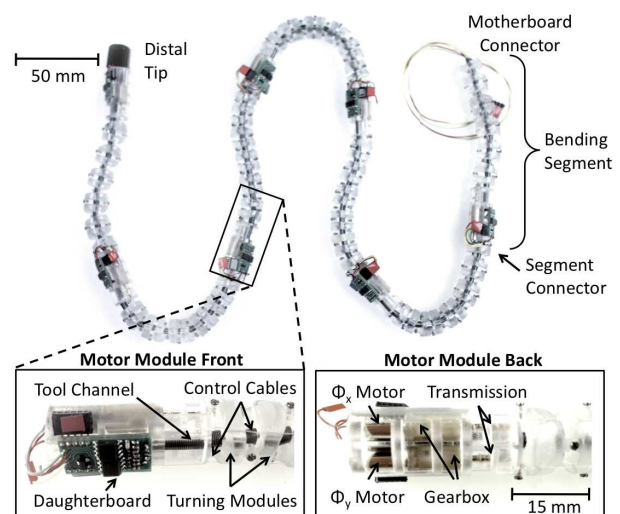


Fig. 1. A modular multi-segment continuum robotic endoscope is shown without the outer sheath. Here, seven segments are shown with an overall length of 0.91 m. The design is easily extended by plugging in additional bending segments. Each modular bending segment contains an electronics daughterboard and motors that pull cables in order to turn each segment.

Manuscript received Feb. 4th, 2013 for the IEEE ICRA Conference.

Y. Chen, J. Liang and I. W. Hunter are with the BioInstrumentation Lab in the Department of Mechanical Engineering, Massachusetts Institute of Technology, Cambridge, MA, U. S. A. (contact: yichen@mit.edu)

Unlike other multi-segment continuum robots [17], [22], [23], [24] which use large actuators at the proximal end and cannot be easily expanded in length, this paper proposes a modular continuum robot design with multiple bending segments, each containing its own actuation motors. Because of the modular nature of the design with the actuation cables enclosed in each segment, the system scales well lengthwise and does not become thicker when more bending segments are added. Our previous work has focused on designing the actuation and sensing for a single robotic bending segment at the tip, which eliminates long Bowden cables [2], [3], [4]. In this paper, we design a robot architecture with multiple modular bending segments which communicate with each other and are independently controlled to produce a long hyper-redundant robotic endoscope, as shown in Fig. 1. We generate kinematic models that can be used to visualize and plan desired trajectories for the robot and we implement the new design to verify our design principles. We then control coordinated bending motions between the segments to help move the endoscope along convoluted paths. This includes an uncoiling motion used for inserting the robot into the body and obtaining lateral scans of the colon walls as well as a follow-the-leader motion that traverses a path emulating the turns in a colon. We show that our modular robotic endoscope is capable of exerting less force on the walls of the colon emulation path than conventional endoscopes.

II. TRAJECTORY GENERATION FOR MODULAR CONTINUUM ENDOSCOPES

For the robotic endoscope application, there are many possible desirable motions that can be helpful during procedures, some of which include a follow-the-leader motion for avoiding colon walls, an uncoiling motion for inserting the endoscope into the body, a linear scanning motion, and a rotary scanning motion for looking at surface features. Each of these motions has a different set of constraints which can be solved to determine the desired sequence of waypoint commands to achieve a given trajectory. In addition, kinematic modeling and simulation are useful for path planning, robot control, as well as visualization of the robot when it is out of view during a procedure.

A. Kinematic Modeling and Simulation

The kinematic model for a twist-restricted continuum robot differs from the model for a non twist-restricted system [4]. In order to simulate and plan paths for the robotic endoscope, the three dimensional orientation of each turning module in a bending segment is modeled in Matlab. Each bending segment includes $N = 11$ turning modules where $N_{odd} = 6$ and $N_{even} = 5$. The overall desired bend angles, as defined by a difference in control cable lengths from the inside of a bend to the outside of a bend, for a single segment m are defined as ϕ_x^m and ϕ_y^m . Euler angles can be defined for the system shown in Fig. 2 as,

$$\zeta^m = \tan(\phi_y^m / \phi_x^m), \quad (1)$$

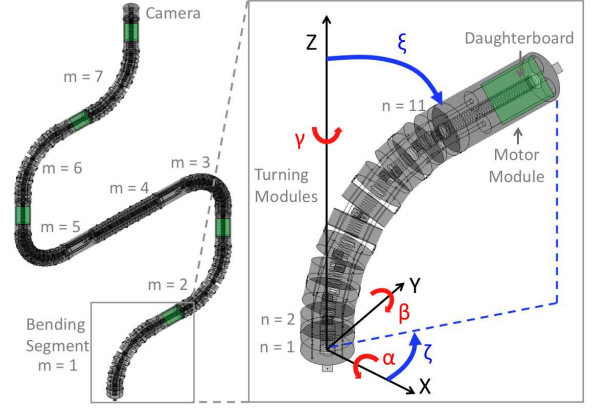


Fig. 2. Simulation of the robotic endoscope with $M = 7$ separate bending sections where each bending section has $N = 11$ turning modules. The coordinate system with yaw, pitch, and roll angles α , β and γ are shown along with Euler angles ζ and ξ .

$$\xi^m = \sqrt{\phi_x^{m2} + \phi_y^{m2}}. \quad (2)$$

The angle ζ^m indicates the relative magnitude between the overall desired bend angles ϕ_x and ϕ_y , while ξ^m indicates the magnitude of deflection.

It is important to note that the cord length angles ϕ_x^m and ϕ_y^m (which could be measured by bend sensors or encoders [4]) are not the same as the angles measured by the gyroscope sensors used in the implementation of the robotic endoscope outlined in this paper. In order to control the full three dimensional rotation of each bending segment, the angles integrated using gyroscope signals also need to be converted to the Euler magnitude angles ζ^m and ξ^m . For a controller that implements x-axis rotations α^m followed by y-axis rotations β^m , the following equality can be used,

$$\mathbf{R}_z(\zeta^m) \mathbf{R}_x(\xi^m) \mathbf{R}_z(-\zeta^m) = \mathbf{R}_z(\gamma^m) \mathbf{R}_y(\beta^m) \mathbf{R}_x(\alpha^m). \quad (3)$$

Note that for simple two dimensional planar motions, it is possible to approximate $\phi_x^m \approx \alpha^m$ for odd units and $\phi_y^m \approx \beta^m$ for even units.

Next, the \mathbf{X}_n^m , \mathbf{Y}_n^m , and \mathbf{Z}_n^m final location of a series of elements associated with the n th segment can be determined from the initial locations \mathbf{X}_i , \mathbf{Y}_i , and \mathbf{Z}_i using a rotation matrix \mathbf{R}_n^m and a translation matrix \mathbf{T}_n^m ,

$$\begin{bmatrix} \mathbf{X}_n^m \\ \mathbf{Y}_n^m \\ \mathbf{Z}_n^m \end{bmatrix} = \mathbf{R}_n^m \begin{bmatrix} \mathbf{X}_i \\ \mathbf{Y}_i \\ \mathbf{Z}_i \end{bmatrix} + \mathbf{T}_n^m. \quad (4)$$

Since rotational joints were added to prevent twisting motions, each turning module can only rotate in one of the two bending angles and are offset from the control cables by $\zeta_n^m = 45^\circ$. The Euler angles associated with each turning module n , where n is odd, are defined by $\xi_n^m \approx \xi^m \cos(\zeta_m - \zeta_n^m) / N_{odd}$ and,

$$\mathbf{R}_n^m = \mathbf{R}_z(\zeta_n^m) \mathbf{R}_x(\xi_n^m) \mathbf{R}_z(-\zeta_n^m) \mathbf{R}_{n-1}^m. \quad (5)$$

For each turning module n that is even, the rotations are defined by $\xi_n^m \approx \xi^m \sin(\zeta_m - \zeta_n^m)/N_{even}$ and,

$$\mathbf{R}_n^m = \mathbf{R}_z(\zeta_n^m) \mathbf{R}_y(\xi_n^m) \mathbf{R}_z(-\zeta_n^m) \mathbf{R}_{n-1}^m, \quad (6)$$

where the rotations are,

$$\mathbf{R}_z(\theta) = \begin{bmatrix} \cos(\theta) & \sin(\theta) & 0 \\ -\sin(\theta) & \cos(\theta) & 0 \\ 0 & 0 & 1 \end{bmatrix}, \quad (7)$$

$$\mathbf{R}_y(\theta) = \begin{bmatrix} \cos(\theta) & 0 & -\sin(\theta) \\ 0 & 1 & 0 \\ \sin(\theta) & 0 & \cos(\theta) \end{bmatrix}, \quad (8)$$

$$\mathbf{R}_x(\theta) = \begin{bmatrix} 1 & 0 & 0 \\ 0 & \cos(\theta) & \sin(\theta) \\ 0 & -\sin(\theta) & \cos(\theta) \end{bmatrix}. \quad (9)$$

Each simulated element is first rotated by the rotation defined by the previous element \mathbf{R}_{n-1}^m and then rotated by $-\zeta_n^m$, bent by ξ_n^m and then rotate back by ζ_n^m .

B. Output Force and Endpoint Stiffness

The output force normal to the tip of a bending segment can be used to determine the endpoint stiffness of each bending segment of the robot. The output force normal to the tip F_{ext} is,

$$F_{ext} = \frac{\phi}{L_s} F_{in} e^{-\mu\phi} - K\phi. \quad (10)$$

The pull force of the motor F_{in} is modified by the capstan friction of the bending angle ϕ and the coefficient of friction μ . The internal normal force from string tension is related to the tangential string tension through the radius of curvature of the bent segment ϕ/L_s , which is a function of the length of the bending segment L_s . Lastly, the endoscope structural stiffness K is included.

From this equation, it is clear that the output force normal to the tip is zero when the bending angle is near zero. Therefore, the endpoint stiffness near low bending angles will be very small. When generating trajectories, configurations that require perfectly straight angles are penalized. Paths with many straight bending segments will also require an additional straightening algorithm in order to achieve the desired configuration. The kinematic model can be used to describe the location of each element and to coordinate path planning while the tip force model provides insights on the configurations with the lowest endpoint stiffness.

C. Uncoiling Path Planning

The uncoiling mode can be used to insert the robotic endoscope into the body or move the endoscope for linear scanning. Other robotic endoscope designs commonly use a separate long linear actuator for this purpose [20] or a separate extension or inchworm actuator. In our case, since each segment is motorized, a coordinated uncoiling motion can be used to insert the endoscope into the body following a set of constraints. For planar motions,

$$\sum_m^{M_{uncoil}} \phi_x^m = \phi_{xd} \quad \text{and} \quad \sum_m^{M_{uncoil}} \phi_y^m = \phi_{yd}. \quad (11)$$

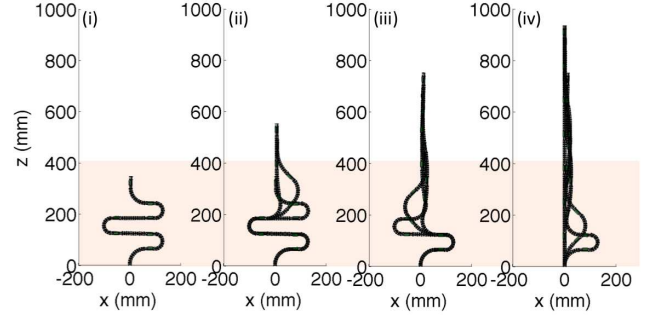


Fig. 3. The uncoiling algorithm for robotic endoscope insertion is shown with a simulation for $M = 7$ bending sections. The uncoiling order goes from left to right and the highlighted area denotes the uncoiling region.

The sum of all the turning angles for segments within the uncoiling region M_{uncoil} must be equal to the final desired angles ϕ_{xd} and ϕ_{yd} . Note that $2\pi n$ multiples of ϕ_{xd} or ϕ_{yd} satisfy configuration constraints but require more complex 3D rotations for uncoiling. In addition, the location of the point within the uncoiling region must be $X^{M_{uncoil}} = X_d$ and $Y^{M_{uncoil}} = Y_d$ and length of the robot outside the uncoil region $L^M - L^{M_{uncoil}} = L_d$. One possible uncoiling configurations where $\phi_{xd} = 0$, $\phi_{yd} = 0$, $X_d = 0$ and $Y_d = 0$ is shown in Fig. 3. By specifying a desired coil length L_d , it is possible to generate a set of waypoints for inserting the robotic endoscope into the body without a separate insertion actuator. There are many possible algorithms that can satisfy the constraints. In this case, the algorithm we use chooses to sequentially uncoil the three segments closest to the exit point. This algorithm uses the fewest number of actuators at any one time to complete the desired task. In order to provide a higher endpoint stiffness, the algorithm avoids bending angles with magnitudes less than 7° .

D. Follow-the-Leader Path Planning

A follow-the-leader mode can be used to navigate the inside of the colon by following a defined set of bends dictated by the lead bending segment. These bends are then followed by all the subsequent segments when they reach the same position. These bends may come from x-ray, fluoroscopy, ultrasound and other scans. Alternatively, the bends can be defined as the operators are working in real time such that they can push the endoscope forward, choose to turn the tip of the endoscope, and have all subsequent bending sections follow the same turns.

The set of bends for the final configuration are defined such that $\Phi_{xd}(mL_s) = \phi_{xd}^m$ and $\Phi_{yd}(mL_s) = \phi_{yd}^m$, where each bending segment is L_s long. Ideally, each desired bend is large enough to accommodate two or more bending segments to form a more continuous shape and to reduce deviations from the desired shape. Next, a function is created to interpolate between the desired bends for segments that have entered the body $L_d > (m+1)L_s$,

$$\phi_x^m(L_d) = f(\Phi_{xd}(L_d - (m+1)L_s)) \quad (12)$$

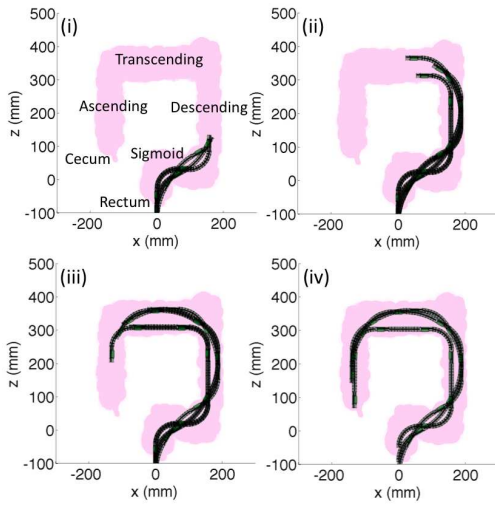


Fig. 4. The follow-the-leader algorithm simulation shows how the robotic endoscope can be used to traverse a convoluted path. The simulation uses $M = 7$ bending sections with several different desired lengths L_d are shown together on the same plot. The follow-the-leader order goes from left to right and from top to bottom with the shape of a colon highlighted in pink for reference. Different parts of the colon, including the rectum, sigmoid, descending, transverse, ascending, and cecum are labeled.

For regions outside the body, other algorithms like uncoiling can be used or the controller can simply be turned off. An interpolation function $f(\bullet)$ can be used to generate intermediate waypoints. Linear interpolation works best for angles with magnitudes less than 90° but will also work moderately well for larger angles. More complex functions which allow for overshoot to reduce overall positioning error can also be used. In general, bending angles with magnitudes less than 7° are avoided for two or more adjacent bending segment in order to provide a higher endpoint stiffness.

A simplified path in Fig. 4 that emulates the turns in the colon (excluding colon pleats and three dimensional bends) shows four 90° bends with $M = 7$. The modular nature of the bends creates conformation errors, here the maximum deviation from the basic desired path is about 52 mm for a total desired length of $L_d = 910$ mm. This path planning paradigm provides higher endpoint stiffness, is fast and easy to compute and works for both previously defined paths as well as paths generated during the procedure. This path planning method also has the benefit of being able to modify any of the bends during the procedure if the path constraints happen to change, such as when the patient moves.

III. IMPLEMENTATION

The overall robotic endoscope design can be broken down into several repeated segments as shown in Fig. 1. The mechanical components, electronics, software and communications architecture are designed to be modular so that the endoscope can be lengthened by plugging in additional segments, each containing its own daughterboard, motors and turning modules.

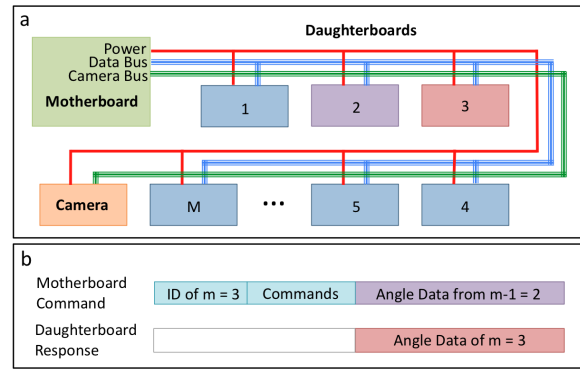


Fig. 5. a) The arrangement of the communication between the modular boards is shown. b) The communication signal from the motherboard to daughterboard $m = 3$ shows how the ID, commands and angles from the previous board are sent.

A. Mechanical Design

Each continuum turning module houses monofilament cables that turn the assembly in ϕ_x and ϕ_y rotations. The turning modules are constructed through a stereolithography process using Accura SI-60 resin. These modules are connected to each other on joints which allow for ϕ_x and ϕ_y rotations but not twisting motions. Through the center of this assembly is a long, 4 mm diameter spring that serves as the tool passage used for passing biopsy tools through the endoscope and for providing a small restoring force.

The turning section is then connected to the motor module which contain two 6 mm diameter motors geared at a ratio of 1:136 and rotary to linear transmissions. Unlike previous designs with lower gear ratios [3], the motors in this design produce higher forces, are not back drivable, and can be treated as angular displacement output devices up to the stall force. Each motor controls one turning axis; rotating the motor shaft in one direction tightens one control cable which then rotates the continuum bending section in one direction while rotating the motor in the opposing direction rotates the bending section in the opposite direction. The complex motor module design with the built in transmission is manufactured using stereolithography and are 15 mm in diameter by 35 mm long. Connectors are placed at the end of the module for the tool passage as well as power and communications wires.

The continuum bending sections and motor modules are repeated to form a long hyper-redundant robot. Each 130 mm long bending segment can bend by 180° . This robot can then be covered with a polymer (e.g. black polyurethane) outer coating to protect it from external contamination and water during a procedure. The distal tip of the robotic endoscope houses a camera and lighting system. The proximal end of the robot is connected to a handle through which power and communications signals are routed.

B. Electronics and Communications

The electronics architecture is composed of a motherboard located at the outside of the robot and several daughter-

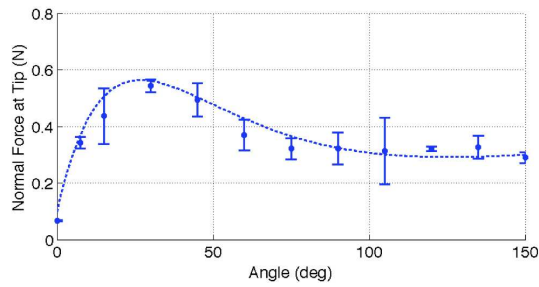


Fig. 6. Normal tip force as a function of bending angle is shown for a single bending segment with motor voltage limited to 3V. The dotted line serves as a guide for the eye.

boards, each of which is located on a motor module. The motherboard provides power, USB communications with a computer and an Arm Cortex M3 micro controller. The electronics design for the daughterboards are small 10×20 mm circuit boards that include an Arm Cortex M3 micro controller, two H-bridge motor drivers, and an Invensense MPU-6000 MEMS gyroscope and accelerometer.

The motherboard communicates with the daughterboards using a serial peripheral interface with all the daughterboards sharing the same output bus as shown in Fig. 5a. The motherboard sends commands to each daughterboard separately using unique IDs and each daughterboard responds by reporting angles integrated on the micro controller. To prevent bus contention, the daughterboard outputs only turn on when their unique IDs are called. The bending angle of each section is determined by the difference between the angles calculated on a module m and the module connected to it $m-1$ as shown by Fig. 5b. Therefore, the motherboard also supplies the angle data from module $m-1$ to module m . The bend angles are then calculated and used for independent closed loop angle control on each segment.

The camera board includes a Toshiba TCM8230MD camera, micro controller and high speed video data serializer. The video data are deserialized on the motherboard side, buffered and sent via high speed USB to the computer. The computer software and user interface controlling the commands to the motherboard and daughterboards is written in C#.

IV. RESULTS

The performance of a single segment as well as the performance of a chain of segments is investigated. The paths generated for coordinated motions are implemented and simulation data are compared with experimental results. A video showing several coordinated motions including the uncoiling motion and follow-the-leader motion is included with the paper. Videos exhibiting other capabilities of the robot including lateral scanning, two dimensional scanning, grasping, and crawling are also shown.

A. Segment Dynamics

The static output force normal to the tip of a bending segment as a function of bending angle is shown in Fig. 6.

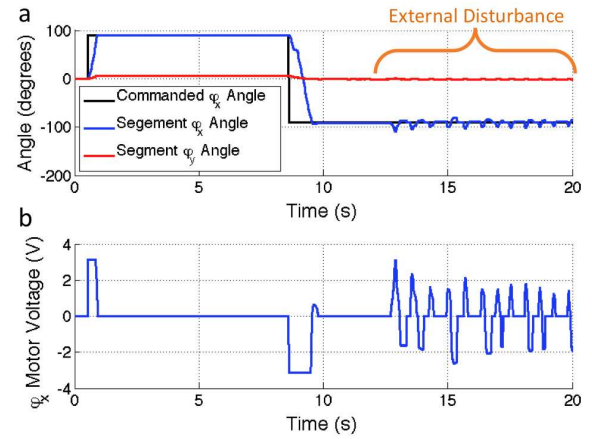


Fig. 7. a) The closed loop response to a command in the ϕ_x bending axis is shown along with disturbance rejection capabilities. b) The voltage output to the ϕ_x motor is shown.

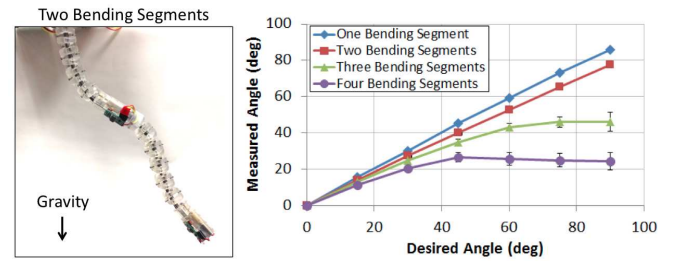


Fig. 8. The ability of the endoscope to lift its own weight is shown with the gravity vector pointing downward. One unit is commanded to go to different angles with zero to three additional units attached to it. The panel on the left shows one additional unit attached (a total of two bending segments). Five tests were conducted for each data point.

As predicted by Equation 10, when the bending angle is near zero, the normal force output is very small leading to a low endpoint stiffness when the bending segments are straight. The maximum output force and endpoint stiffness occurs near 25° to 30° . Based on this information, paths that utilize angles larger than 7° in magnitude will have better disturbance rejection and should therefore be used as a lower limit for path planning algorithms.

A closed loop controller is generated to control the desired ϕ_x and ϕ_y rotations. The controller takes in proportional and derivative gains, performs dead band compensation, and converts the desired output voltage to a PWM signal that is sent to the H-bridge motor controller. The closed loop dynamics of one unloaded segment is shown in Fig. 7. The segment is commanded to bend in 90° and then -90° and then the bending segment is tapped to show disturbance rejection. The 3V output limited slew rate of the module is $250^\circ/s$ and the angle control tolerance is set to 2° . The parasitic rotation in the ϕ_y axis is less than 7%.

The stiffness of the bending segments can also be modulated in this design. When the bending segment is straight with motors off, the stiffness of the endoscope comes from the spring that is used for the tool channel, stiffness of wires, and stiffness of the rotating joints. This baseline stiffness is

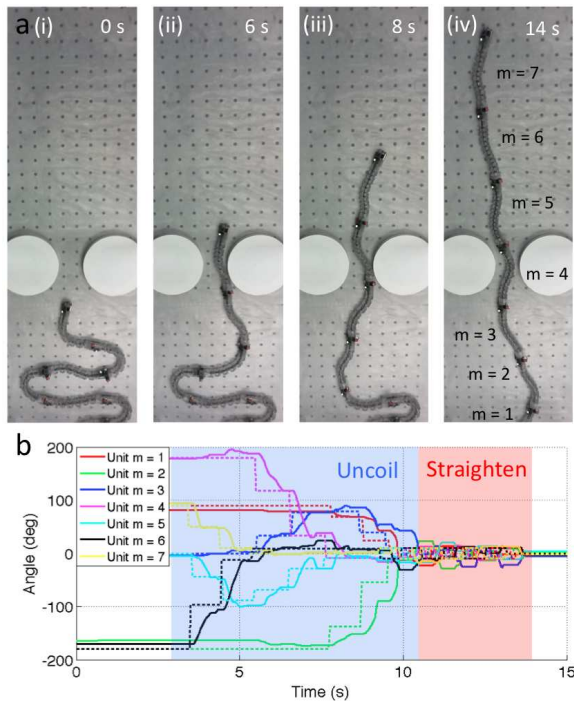


Fig. 9. a) Snapshots of the robot in uncoiling mode are shown extending in order to insert the robot into the body without using additional actuators. The path was planned in Fig. 3. White circular obstacles were added for reference. b) Time series data of the desired bending angles (dotted lines) and measured closed loop bending angles (solid lines) for each of the seven bending segments is shown for the uncoiling and straightening modes.

between 3.0 and 4.1 $mN/^\circ$. When the bending segment is straight with motors on, the stiffness of the endoscope comes from the stiffness of the monofilament cables and the force output of the motors and is between 9.0 and 12.9 $mN/^\circ$. The maximum force output normal to the tip of a single bending section at 3 V is approximately 0.6 N. Since each bending segment has a mass of 22 g, each segment is capable of lifting up to 2.7 times its own weight. Figure 8 shows how gravity effects the ability of the module to rotate to different angles. In this experiment, the base unit hangs freely with gravity pointing down. It is then commanded to different angles with zero to three additional units attached to the end. The final measured angle clearly shows that the effect of lifting one additional unit is small. However, the endoscope can only achieve 20 to 30 degrees of rotation with three units of load (total of four bending segments).

B. Uncoiling Motion

The robot used for the coordinated motion experiments is a seven bending segment robot that is 0.91 m long, has a mass of 157 g, and has 14 degrees of freedom (2 degrees of freedom per segment). For the experimental setups for the coordinated paths, white circular obstacles and a metal table that is covered with a thin teflon sheet to reduce friction is used. Several large increment waypoints are set in order to reduce the effect of static friction. Due to the mass of conjoining segments, the robot's bending speed is much slower

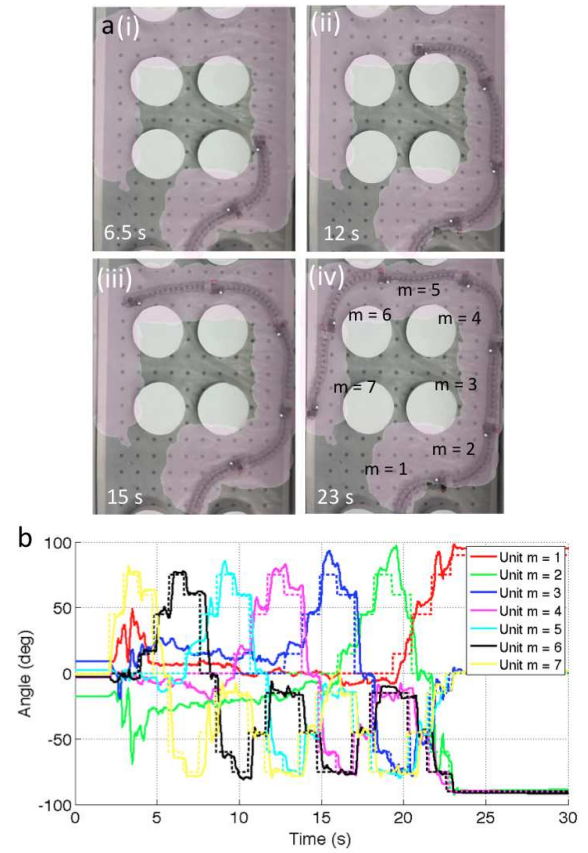


Fig. 10. a) Snapshots of the robot in follow-the-leader mode are shown traversing a path planned in Fig. 4 that emulates the turns in the colon. Different parts of the colon are highlighted in pink. White circular obstacles were added for reference. b) Time series data of both the desired bending angles (dotted lines) and measured closed loop bending angles (solid lines) for each of the seven bending segments is shown.

than that of a single bending segment and the speed can vary from 35°/s to 200°/s. Figure 9 shows the experimental data from the uncoiling path planned earlier in Fig. 3 for insertion into the body without using additional insertion actuators. The desired angles are generally maintained by the controllers on each module. However, external friction, play in the modules, and the overall mass of the system does prevent the robot from achieving all the desired angles perfectly with errors that can be as large as 30 to 40° for units near the proximal end. Despite missing the desired angle at some waypoints, the robot eventually catches up to the desired angle thereby achieving the desired configuration. In general, the robot does a good job of releasing from the coiled state and the angular errors are less than 10°. After the uncoiling state, the robot is not perfectly straight due to low endpoint stiffness for angles near zero degrees. Therefore, a straightening state is added which moves the bending segments back and forth slightly to overcome friction.

C. Follow-the-Leader Motion

A simplified path that emulates the turns in a colon is also tested for the follow-the-leader path planning algorithm. This phantom is designed so that measurements of repeatability

and contact forces can be made while conformation can be clearly assessed and filmed. For these reasons, it does not include tissue contact effects and gravity effects from three dimensional bends. The robot is inserted by hand at a constant speed. Because all bending segments not within the field of view are left uncontrolled, there are large errors especially for units $m = 1$ and $m = 2$ for times less than 15 seconds in Fig. 10. The robot does a good job of replicated the desired shape shown in Fig. 4 which is made up of four turns each 90° in magnitude. The robot transmits much of the insertion resistance down to the endoscope outside the field of view. However, when reaching the top right corner, the robot rebounds off of the right side wall of the setup and rubs against the top left wall slightly.

More rigid closed loop bending segments would transmit more of the forces through the body of the robot and reduce forces exerted on the side walls when the robot changes direction. However, a lower stiffness actually improves the ability of the robot to follow a constrained path, reducing the path errors shown in Fig. 4 and preventing accidental colon wall perforation. A comparison of forces exerted on the walls of the setup are shown in Table I for a Olympus CF-IBW conventional endoscope and the robotic endoscope. Five different tests were conducted for each endoscope and the maximum forces during those tests were collected from each contact point. The means and standard deviations are shown in the table. The maximum forces exerted on the walls of the setup are measured when the endoscopes are allowed to smoothly slide along all the walls. The forces exerted on the walls of the setup are due to several factors including the forces required to change the shape of the endoscope, forces required to move the mass of the endoscope, and forces due to friction. In general, the maximum forces occur at the conformation shown in Fig. 11. The contributions to the forces exerted on the wall at point A include the additional mass of the endoscope as well as the additional forces from sliding friction at points B and C. Therefore, the forces are generally larger at point A than the other points.

The conventional endoscope exerts more force on the external walls (at statistically significant levels p -values $\leq 4.5 \times 10^{-5}$) when attempting to reach the desired shape because the body of the endoscope cannot make independent bends. The conventional endoscope is stiffer requiring a larger force to change the shape of the endoscope. The mass of the conventional endoscope is also higher at 0.320 kg for a length of 910 mm. These factors contribute to the higher forces in Table I. The robotic endoscope can change shape thereby virtually eliminating the forces required to change its conformation. In some cases, the robotic endoscope does not contact wall C. The robotic endoscope is also lighter, reducing the forces exerted on the colon walls.

Repeatability data can also be obtained for these two motions. It is important to note that the robotic endoscope is designed to be flexible (to avoid puncturing the colon walls) and to operate in conjunction with a human operator's motions (such as insertion during a follow-the-leader path

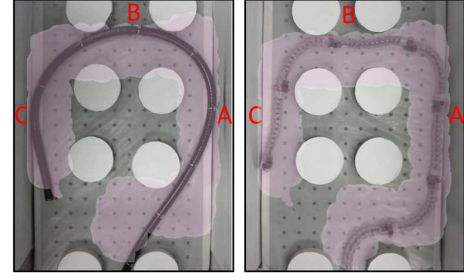


Fig. 11. Conformation of a Olympus CF-IBW endoscope (left) and the continuum robotic endoscope are shown. The normal forces exerted by the endoscopes on the walls are measured at three points A, B and C.

TABLE I

Endoscope	Maximum Force (N) Exerted on Wall		
	A	B	C
Conventional	1.72 ± 0.14	1.69 ± 0.24	1.06 ± 0.38
Robotic	0.34 ± 0.08	0.20 ± 0.04	0.09 ± 0.03

TABLE II

Error	Steady State Tracking Error (degrees)		
	Uncoiling	Straightening	Follow-The-Leader
Mean	2.78 ± 1.12	2.24 ± 1.14	3.63 ± 2.00
Maximum	6.36 ± 2.77	4.95 ± 2.64	9.85 ± 4.03
Inter-Trial	1.72 ± 1.12	1.47 ± 1.20	3.62 ± 2.26

TABLE III

Frame	Steady State Position Range (mm)			
	Uncoiling		Follow-The-Leader	
	Tip	Body	Tip	Body
(i)	35.3	20.7	39.3	32.3
(ii)	47.2	47.3	28.1	27.5
(iii)	68.8	47.8	38.8	59.5
(iv)	44.7	43.7	37.1	36.7

plan), and therefore position repeatability is not paramount. Here, test fields are designed to be relatively open and prevent the robot from relying on walls for reducing the trial-to-trial variation. Repeatability data for angle tracking from gyroscope readings is shown in Table II. The steady state tracking error from the desired path is collected from each experiment and the average of all seven bending segments across five independent tests is shown in the first row. The maximum error of each experiment is also shown along with the inter-trial (or trial-to-trial) variation. This shows that the angle tracking is typically 1 to 4 degrees with the follow-the-leader path producing the largest angle tracking errors.

The corresponding positioning data from video data is shown in Table III. Each experiment was completed five times and the video data was overlapped. Four frames of interest were chosen, similar to the four frames shown in Figures 9 and 10. The maximum range of the tip and body motions for those four frames are then measured. The majority of the variation for the uncoiling motion occurs towards the end of the uncoiling and is eventually corrected by utilizing the straightening algorithm. The tip tends to produce more position variation than any other point on

the body. For the follow-the-leader motion, the majority of the position variation is due to the operator insertion and is highest at frame (iii). The typical position variation is 30 to 40 mm.

V. CONCLUSION

This paper outlines the design of a modular continuum robotic endoscope design. Unlike previous work that used large actuators at the proximal end of the endoscope [17], this design is modular such that each bending segment has its own set of actuators, micro controller, gyroscope and motor drivers. These sections can be individually controlled using our communications protocol to form a scalable robotic endoscope design that does not require any large external actuators for insertion or for bending the continuum segments. Kinematic modeling is performed for the turning modules in each bending segment and two path planning algorithms for uncoiling and follow-the-leader motions are outlined and simulated. Paths were generated to penalize straight motions in order to increase the endpoint stiffness of each desired configuration. The closed loop performance of the bending segments is shown as well as the performance of the robot using waypoints generated by the path planning algorithms.

There are many possible extensions for this hyper-redundant modular continuum robotic endoscope design. Future work includes the investigation of additional coordinated motions that may be useful for physicians including a more compact uncoiling algorithm, rotational scanning, grasping and propulsion modes. In particular, three-dimensional paths and more advanced phantoms that better simulate human colons [9], [10] can be explored by employing a larger number of bending segments. Additional effects such as gravity, friction, tissue contact, and folds in the colon walls will also be considered.

ACKNOWLEDGMENT

The authors acknowledge Jillian M. Oliveira, Shigehiko Tanaka and Al Couvillon for their previous work on the project. The project partially was supported by the Department of Defense (DoD) through the National Defense Science & Engineering Graduate Fellowship (NDSEG) Program, 32 CFR 168a.

REFERENCES

- [1] F. Renda and C. Laschi, "A general mechanical model for tendon-driven continuum manipulators," in *Proceedings of the 2012 IEEE International Conference on Robotics and Automation*, pp. 3813–3818, 2012.
- [2] Y. Chen, S. Tanaka, and I. W. Hunter, "Disposable endoscope tip actuation design and robotic platform," in *Proceedings of the 32nd Annual International Conference of the IEEE Engineering in Medicine and Biology Society*, pp. 2279–2282, 2010.
- [3] Y. Chen, J. M. Oliveira, and I. W. Hunter, "Sensor architecture for a two-actuator robotic endoscope tip," in *Proceedings of the 33rd Annual International Conference of the IEEE Engineering in Medicine and Biology Society*, pp. 8340–8343, 2011.
- [4] Y. Chen, J. M. Oliveira, and I. W. Hunter, "Two-axis bend sensor design, kinematics and control for a continuum robotic endoscope," in *Proceedings of the 2013 IEEE International Conference on Robotics and Automation*, pp. 696–702, 2013.
- [5] F. Cepolina and R. C. Michelini, "Review of robotic fixtures for minimally invasive surgery," *International Journal of Medical Robotics and Computer Assisted Surgery*, vol. 1, no. 1, pp. 43–63, 2004.
- [6] K. Wang, G. Yan, G. Ma, and D. Ye, "An earthworm-like robotic endoscope system for human intestine: Design, analysis, and experiment," *Annals of Biomedical Engineering*, vol. 37, no. 1, pp. 210–221, 2009.
- [7] D. Glozman, N. Hassidov, M. Senesh, and M. Shoham, "A self-propelled inflatable earthworm-like endoscope actuated by single supply line," *IEEE Transactions on Biomedical Engineering*, vol. 57, no. 6, pp. 1264–1272, 2010.
- [8] J. Peirs, D. Reynaerts, and H. Van Brussel, "A miniature manipulator for integration in a self-propelling endoscope," *Sensors and Actuators A*, vol. 92, pp. 343–349, 2001.
- [9] K. Ozaki, S. Wakimoto, K. Suzumori, and Y. Yamamoto, "Novel design of rubber tube actuator improving mountability and drivability for assisting colonoscopy insertion," in *Proceedings of the 2011 IEEE International Conference on Robotics and Automation*, pp. 3263–3268, 2011.
- [10] T. Yanagida, K. Adachi, M. Yokojima, and T. Nakamura, "Development of a peristaltic crawling robot attached to a large intestine endoscope using bellows-type artificial rubber muscles," in *Proceedings of the 2012 IEEE International Conference on Intelligent Robots and Systems*, pp. 2935–2940, 2012.
- [11] H. Yamamoto, "Double-balloon endoscopy," *Clinical Gastroenterology and Hepatology*, vol. 3, no. 7, pp. S27–S29, 2005.
- [12] P. Valdastrì, M. Simi, and R. J. Webster III, "Advanced technologies for gastrointestinal endoscopy," *Annual Review of Biomedical Engineering*, vol. 14, pp. 397–429, 2012.
- [13] J. K. Hopkins, B. W. Spranklin, and S. K. Gupta, "A survey of snake-inspired robot designs," *Bioinspiration and Biomimetics*, vol. 4, p. 021001, 2009.
- [14] K.-W. Kwok, K. H. Tsoi, V. Vitiello, J. Clarke, G. C. T. Chow, W. Luk, and G.-Z. Yang, "Dimensionality reduction in controlling articulated snake robot for endoscopy under dynamic active constraints," *IEEE Transactions on Robotics*, vol. 29, no. 1, pp. 15–31, 2013.
- [15] C. Wright, A. Buchan, B. Brown, J. Geist, M. Schwerin, D. Rollinson, M. Tesch, and H. Choset, "Design and architecture of the unified modular snake robot," in *Proceedings of the 2012 IEEE International Conference on Robotics and Automation*, pp. 4347–4354, 2012.
- [16] A. M. Andruska and K. S. Peterson, "Control of a snake-like robot in an elastically deformable channel," *IEEE/ASME Transactions on Mechatronics*, vol. 13, no. 2, pp. 219–227, 2008.
- [17] A. Eickhoff, R. Jakobs, A. Kamal, S. Mermash, J. F. Riemann, and J. van Dam, "In vitro evaluation of forces exerted by a new computer-assisted colonoscopy (the NeoGuide Endoscopy System)," *Endoscopy*, vol. 38, no. 12, pp. 1224–1229, 2006.
- [18] A. Eickhoff, J. van Dam, R. Jakobs, V. Kudis, D. Hartmann, U. Damian, U. Weickert, D. Schilling, and J. F. Riemann, "Computer-assisted colonoscopy (the NeoGuide Endoscopy System): results of the first human clinical trial ("PACE study")," *American Journal of Gastroenterology*, vol. 102, no. 2, pp. 261–266, 2007.
- [19] K. Sumiyama, M. Kaise, T. Nakayoshi, M. Kato, T. Mashiko, Y. Uchiyama, K. Goda, S. Hino, Y. Nakamura, K. Matsuda, K. Mochizuki, M. Kawamura, and H. Tajiri, "Combined use of a magnifying endoscope with a narrow band imaging system and a multibending endoscope for en bloc EMR of early stage gastric cancer," *Gastrointestinal Endoscopy*, vol. 60, no. 1, pp. 79–84, 2004.
- [20] T. Ota, A. Degani, D. Schwartzman, B. Zubiate, J. McGarvey, H. Choset, and M. A. Zenati, "A highly articulated robotic surgical system for minimally invasive surgery," *The Annals of Thoracic Surgery*, vol. 87, pp. 1253–1256, 2009.
- [21] A. Degani, H. Choset, A. Wolf, and M. Zenati, "Highly articulated robotic probe for minimally invasive surgery," in *Proceedings of the 2006 IEEE International Conference on Robotics and Automation*, pp. 4167–4172, 2006.
- [22] I. D. Walker, "Continuous backbone "continuum" robot manipulators," *ISRN Robotics*, vol. 2013, p. 726506, 2013.
- [23] B. A. Jones and I. D. Walker, "Kinematics for multisection continuum robots," *Transactions on Robotics*, vol. 22, no. 1, pp. 43–57, 2006.
- [24] A. Bajo, R. E. Goldman, and N. Simaan, "Configuration and joint feedback for enhanced performance of multi-segment continuum robots," in *Proceedings of the 2011 IEEE International Conference on Robotics and Automation*, pp. 2905–2912, 2011.